Advancing thermoelectrics by suppressing deep-level defects in Pb-doped $AgCrSe_2$ alloys

Yadong Wang(王亚东)[1,†], Fujie Zhang(张富界)[1,†], Xuri Rao(饶旭日)[1], Haoran Feng(冯皓然)[1], Liwei Lin(林黎蔚)[1,‡], Ding Ren(任丁)[1], Bo Liu(刘波)[1], and Ran Ang(昂然)[1,2,§]

[1] *Key Laboratory of Radiation Physics and Technology, Ministry of Education, Institute of Nuclear Science and Technology, Sichuan University, Chengdu* 610064, *China*

[2] *Institute of New Energy and Low-Carbon Technology, Sichuan University, Chengdu* 610065, *China*

(Received 28 November 2022; revised manuscript received 17 January 2023; accepted manuscript online 31 January 2023)

$AgCrSe_2$-based compounds have attracted much attention as an environmentally friendly thermoelectric material in recent years due to the intriguing liquid-like properties. However, the ultra-low carrier concentration and the high Ag_{Cr} deep-level defects limit the overall thermoelectric performance. Here, we successfully introduced Pb into Ag-deficient $Ag_{0.97}CrSe_2$ alloys to tune the carrier concentration across a broad temperature range. The Pb^{2+} as an acceptor dopant preferentially occupies Cr sites, boosting the hole carrier concentration to 1.77×10^{19} cm^{-3} at room temperature. Furthermore, the Pb strongly inhibits the creation of intrinsic Ag_{Cr} defects, weakens the increased thermal excited ionization with the increasing temperature and slowed the rising trend of the carrier concentration. The designed carrier concentration matches the theoretically predicted optimized one over the entire temperature range, leading to a remarkable enhancement in power factor, especially the maximum power factor of ~ 500 $\mu W\cdot m^{-1}\cdot K^{-2}$ at 750 K is superior to most previous results. Additionally, the abundant point defects promote phonon scattering, thus reducing the lattice thermal conductivity. As a result, the maximum figure of merit zT (~ 0.51 at 750 K) is achieved in $Ag_{0.97}Cr_{0.995}Pb_{0.005}Se_2$. This work confirms the feasibility of manipulating deep-level defects to achieve temperature-dependent optimal carrier concentration and provides a valuable guidance for other thermoelectric materials.

Keywords: $AgCrSe_2$, deep-level defects, carrier concentration modulation, thermoelectric properties

PACS: 72.15.Jf, 73.50.Lw, 74.25.fc, 74.25.fg **DOI:** 10.1088/1674-1056/acb765

1. Introduction

With the continuous consumption of non-renewable energy and the looming energy crisis, it is imperative to implement sustainable development strategies.[1] Thermoelectric materials can directly convert waste heat into electric energy through the Seebeck effect, which has attracted much attention in recent years. The conversion efficiency of thermoelectric materials is limited by dimensionless thermoelectric merit, $zT = S^2\sigma T/(\kappa_e + \kappa_L)$, where S, σ, T, κ_L and κ_e are the Seebeck coefficient, the electrical conductivity, the absolute temperature, and the lattice and electrical components of total thermal conductivity κ, respectively. Outstanding thermoelectric performance requires the simultaneous improvement of electrical transport properties and reduction of thermal conductivity. However, it is difficult to improve the thermoelectric performance by improving a single parameter, due to the strongly coupling of S, σ, and κ_e through carrier concentration.[2]

In the past decades, several effective strategies have been proven and successfully developed for high zT materials such as PbTe,[3,4] GeTe,[5,6] Mg_3Sb_2[7–9] and half-Heusler.[10,11] It can be summarized into two major approaches: carrier concentration modulation,[12] band engineering,[13] energy filtering,[14] etc. are devoted to optimizing electrical transport to improve material power factor PF; defect engineering,[15,16] complex crystal structure,[17,18] liquid-like effects,[19,20] etc. are employed to reduce the only independent parameter of κ_L. Specially, due to the atomic disorder and anharmonicity, superionic conductors with liquid-like effect inherently have low κ_L and are considered as promising thermoelectric materials, such as Ag_2Te,[21,22] $Ag_9(Ga,Al)Se_6$,[23,24] Cu_2Se.[25–27] The common feature is that they are composed of two special sublattices, i.e., a liquid sublattice composed of moving ions and a rigid sublattice composed of fixed ions.

$AgCrSe_2$ is another typical superionic conductor whose layered structure and liquid-like effect have been studied for a long time.[28–30] Common $AgCrSe_2$ is a typical hexagonal layered compound whose crystal structure can be regarded as alternating Ag layers and $CrSe_6$ layers octahedral substructure along the c-axis,[31] and undergoes a phase transition around 450 K.[32–34] Below the superionic transition temperature, $AgCrSe_2$ adopts space group $R3m$. All Ag ions occupy the tetrahedral α sites coordinated by Se atoms, separating the layers of $CrSe_6$ octahedra. While above this temperature, Ag ions undergo disordering with equal probability between the α sites and the symmetry equivalent β sites, and the space group

[†]These authors contributed equally.

[‡]Corresponding author. E-mail: linliwei@scu.edu.cn

[§]Corresponding author. E-mail: rang@scu.edu.cn

© 2023 Chinese Physical Society and IOP Publishing Ltd

becomes R-3m.[35] Because of the layered structure and liquid-like effect, $AgCrSe_2$ has an ultra-low lattice thermal conductivity ~ 0.5 W·m^{-1}·K^{-1}.[36] Nevertheless, the extremely low carrier concentration $\sim 10^{17}$ cm^{-3} at room temperature still severely limits the effective carrier transport, resulting in a poor power factor of ~ 70 μW·m^{-1}·K^{-2}. As the temperature increases, its abundant intrinsic deep energy defect levels will gradually ionize, the rapidly soaring carrier concentration seriously deteriorates the thermoelectric performance at high temperatures.[37]

Until now, numerous electronic structure modulations and phonon scattering optimization strategies have been utilized to enhance the thermoelectric properties of $AgCrSe_2$-based materials. Adjusting Ag vacancies by non-stoichiometric doping has been demonstrated as an efficient method to increase the carrier concentration.[36,37] Moreover, the doping of Sb/Bi at the Cr sites can reduce the effective mass as well as optimize the carrier concentration.[29] Notably, the optimal carrier concentration $p_{H,opt}$ is a dynamic temperature-dependent parameter, following $p_{H,opt} \sim (m^*T)^{1.5}$, where m^* is the density of state effective mass.[38] Only when the measured Hall carrier concentration p_H is temperature-dependent and matches the $p_{H,opt}$, a large PF can be obtained over the whole temperature region.[12] The introduction of magnetic nanoparticles and synergistic shallow-deep defect levels facilitate a temperature-dependent trap-reactivation process of carriers, enabling efficient modulation of the carrier concentration and high thermoelectric performance across a broad temperature range.[12,39] Fortunately, the temperature-dependent intrinsic carrier concentration of $AgCrSe_2$ provides the possibility to modulate Ag_{Cr} deep-level impurity states by simple doping, i.e., promoting low carrier concentration at room temperature and suppressing the higher concentration at medium and high temperatures. Additionally, both the solid solution of similarly structured compounds and secondary phase precipitates in $AgCrSe_2$ show enhanced phonon scattering effects, further reducing the κ_L.[28,40]

In this work, we have investigated the influence of Pb doping on the thermoelectric properties of $Ag_{0.97}CrSe_2$ with Ag vacancies on the basis of the above requirements. The Pb^{2+} is introduced as an acceptor dopant into the Cr sites, which increases p_H from 3×10^{18} cm^{-3} to 1.77×10^{19} cm^{-3} at room temperature. Simultaneously, the Pb doping mitigates the influence of the intrinsic Ag_{Cr} deep-level defects, and flattens the increasing trend of p_H with temperature. At higher temperatures, the impurity levels are fully ionized, and the bipolar effect leads to a further slow rising in p_H. The obtained p_H closely matches the $p_{H,opt}$ predicted by the single parabolic band (SPB) model, resulting in an increase of the maximum PF from ~ 340 μW·m^{-1}·K^{-2} to ~ 500 μW·m^{-1}·K^{-2}, which is better than most previous results. Additionally, the Pb doping introduces additional point defect scattering, which decreases the κ_L even more in the whole temperature range. This work effectively manipulates the deep-level defects and optimizes the p_H across the whole temperature range, providing a precious reference for other thermoelectric materials.

2. Experimental details

High purity elements ($> 99.99\%$) were weighed according to the nominal composition of $Ag_{0.97}Cr_{1-x}Pb_xSe_2$ ($x = 0$, 0.25%, 0.5%, 0.75%, and 1%). According to preliminary experiments, we set the nominal composition of the optimal Ag vacancy to 0.97. Then, the mixture was sealed in a quartz tube under a high vacuum. The quartz tubes were slowly heated to 1373 K and held for 48 h, and then gradually cooled to room temperature. The synthesized sample was then ground into powder using a mortar and pestle and hot pressed in a graphite die at 773 K for 30 min with the pressure set at 50 MPa. Subsequently, the square samples (6 mm×6 mm×1 mm) and strip samples (3 mm×2 mm×9 mm) were prepared for thermal and electrical performance measurements, respectively. Due to the presence of $AgCrSe_2$ anisotropy, the thermoelectric properties were measured perpendicular to the hotpressing direction. Powder x-ray diffraction (PXRD) was performed with Cu $K\alpha$ radiation. Microstructure and phase composition were probed with the scanning electron microscopy (SEM, JEOL 7100) equipped with energy dispersive spectrometry (EDS). The electrical conductivity σ and the Seebeck coefficient S were measured by the CTApro apparatus (Beijing Cryoall Science and Technology Co. Ltd) under helium atmosphere. The Hall coefficient (R_H) was measured with the van der Pauw technique at a reversible magnetic field of 1.5 T. The thermal conductivity was calculated via the relationship $\kappa = DC_pd$, where D is the thermal diffusivity measured by the laser flash system (LFA 467, Netzsch); C_p is the heat capacity at constant pressure, which is calculated using the Dulong–Petit law; and d is the density of samples obtained using the Archimedes principle.

3. Results and discussion

Room-temperature PXRD pattern of $Ag_{0.97}Cr_{1-x}Pb_xSe_2$ ($x = 0$, 0.25%, 0.5%, 0.75%, and 1%) is shown in Fig. 1(a). All Bragg diffraction peaks are well matched to the trigonal $AgCrSe_2$ with a $R3m$ space group (PDF#74-0195), and no distinct impurity phase peaks are detected within the XRD detection limit. It can also be found that the diffraction peak intensities of all samples are clearly distinguished from those of the standard card, especially the stronger diffraction in the (00l) direction, which is attributed to the more exposure of a certain crystal plane due to the special hot melt phasing-reheat pressing process. Moreover, no obvious shift is observed in the magnified main diffraction peak (see Fig. S2), which is consistent with the almost constant lattice parameters obtained

by structural Rietveld refinement [see Fig. 1(b)]. Note the strange crystal structure of $AgCrSe_2$, the schematic diagram is displayed in the inset of Fig. 1(b), Cr^{3+} and Ag^{+} have weak bonding with Se^{2-} anions, the occupation of Pb at their sites is random. These synergistical result in the doping of Pb^{2+}, which has a moderate ionic radius (1.19 Å) compared to Cr^{3+} (0.615 Å) and Ag^{+} (1.26 Å),[41–43] has less effect on the lattice parameters.

In order to further observe the microstructure and confirm the effective solid solution of Pb for the $Ag_{0.97}Cr_{1-x}Pb_xSe_2$ samples, the SEM and the corresponding EDS are performed. As shown in Fig. 1(c), the transgranular fracture surface exhibits the typical layered ordered structure of $AgCrSe_2$-based materials, while the macroscopic disorder is attributed to the polycrystalline preparation process, verifying the unusual performance of the XRD peak intensity. The EDS composition mappings demonstrate that all elements are evenly distributed without apparent accumulation, indicating that the Pb is successfully solidified into the $AgCrSe_2$ matrix.

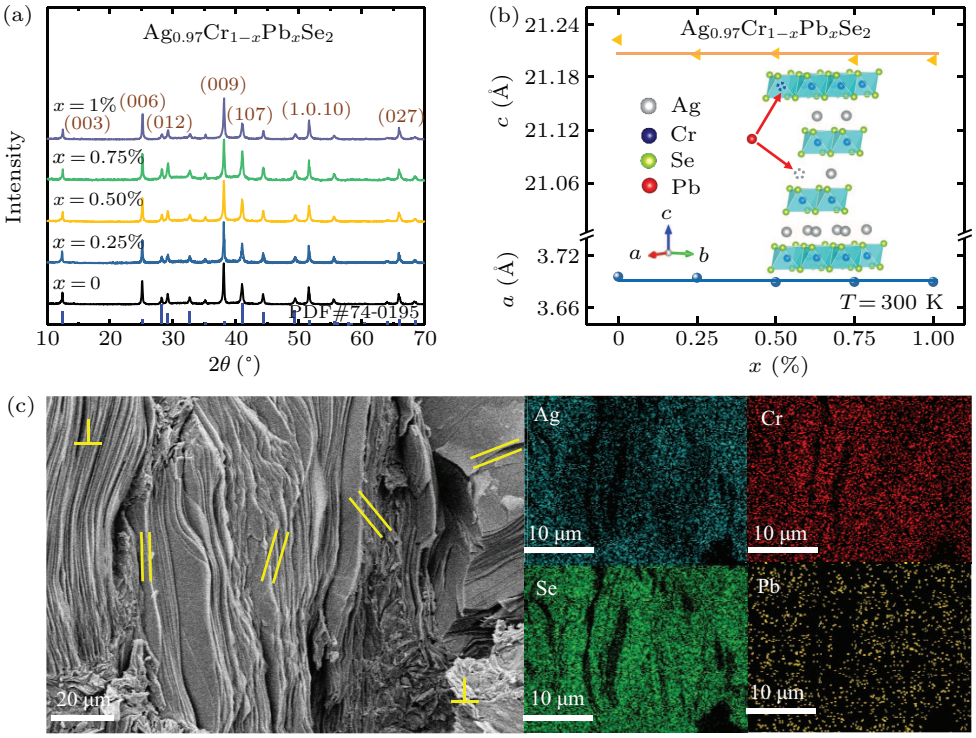


Fig. 1. (a) The room temperature powder XRD patterns, (b) the Pb doping concentration dependent lattice parameters with the room temperature crystal structure for $Ag_{0.97}Cr_{1-x}Pb_xSe_2$ samples and (c) SEM image of the cross-section and the EDS composition mappings for the $Ag_{0.97}Cr_{1-x}Pb_xSe_2$ ($x = 0.5\%$) sample.

The electrical transport properties for $Ag_{0.97}Cr_{1-x}Pb_xSe_2$ samples are displayed in Fig. 2. The electrical conductivity σ of both pristine $AgCrSe_2$ and $Ag_{0.97}CrSe_2$ increases monotonically with the increasing temperature [see Fig. 2(a)], exhibiting typical non-degenerate semiconductor behavior, which is associated with the intrinsic high concentration of Ag_{Cr} deep-level defects even under nominal Ag deficiency. For Pb-doped samples, the σ is significantly improved, and exhibits a degenerate semiconductor behavior below 450 K that decreases with elevating temperature. Interestingly, the σ in the near-room-temperature region decreases gradually with the increase of the Pb doping content, but it is still higher than that of pristine $Ag_{0.97}CrSe_2$. The trend of σ can be explained by the room-temperature Hall measuring results shown in Fig. 2(c). About 0.25% of Pb^{2+} as an electron acceptor occupies Cr sites and efficiently increases the carrier concentration p_H to 1.77×10^{19} cm^{-3}, and due to the abundant Ag vacancies in the matrix, further Pb doping tends to occupy Ag sites, resulting in a decrease in p_H. However, increasing occupation of Ag sites by Pb^{2+} leads to the poor-Cr behavior of the matrix and produces more Cr vacancies that provide additional hole carriers to delay the decrease in p_H. The evolution trend of Hall mobility μ_H is completely opposite to that of p_H, the lower p_H, the higher μ_H, which may be due to the dominance of the ionized impurity scattering and inter-carrier scattering.

Figure 2(b) shows that the Seebeck coefficients S of all samples are synchronously anti-correlated with the conductivity. The increased p_H leads to a worsened S near room temperature, while it is well maintained in the medium and high-temperature regions, which enables a higher PF. Herein, to understand the potential origin of the varying S, the well-established Pisarenko curves based on the SPB model are plotted in Fig. 2(d). It can be clearly seen that the data are well predicted over a wide range of p_H. The data points for all samples fall stably around the theoretically predicted curve with a definite effective mass m^*, indicating a negligible effect of the Pb

doping on the band structure of $Ag_{0.97}Cr_{1-x}Pb_xSe_2$.

For further understanding of the transport properties of the Pb-doped $AgCrSe_2$, the SPB model is employed to predict the thermoelectric properties.[44,45] According to the model, S, μ_H, and PF can be calculated by the following equations:

$$S = \pm\frac{k_B}{e}\left[\eta - \frac{(r+5/2)F_{r+3/2}(\eta)}{(r+3/2)F_{r+1/2}(\eta)}\right], \tag{1}$$

$$\mu_H = \frac{\sqrt{2}eh^4}{48\pi^3 E_{def}^2 m^{*2.5} k_B T^{1.5} F_{1/2}(\eta)}\frac{v_l^2 d}{}\frac{F_{r+1/2}(\eta)}{}, \tag{2}$$

$$PF = \frac{k_B^2}{e^2}\left[\eta - \frac{(r+5/2)F_{r+3/2}(\eta)}{(r+3/2)F_{r+1/2}(\eta)}\right]^2 \times \frac{e^2 h v_l^2 d}{3\pi^2 m^* E_{def}^2} F_{r+1/2}(\eta), \tag{3}$$

where $F_j(\eta)$, v_l, d, E_{def} and r are the Fermi integral, the longitudinal sound velocities, the density, the deformation potential coefficient, and the scattering factor. Obviously, these parameters are closely related to the Fermi level determined by the carrier concentration p_H.

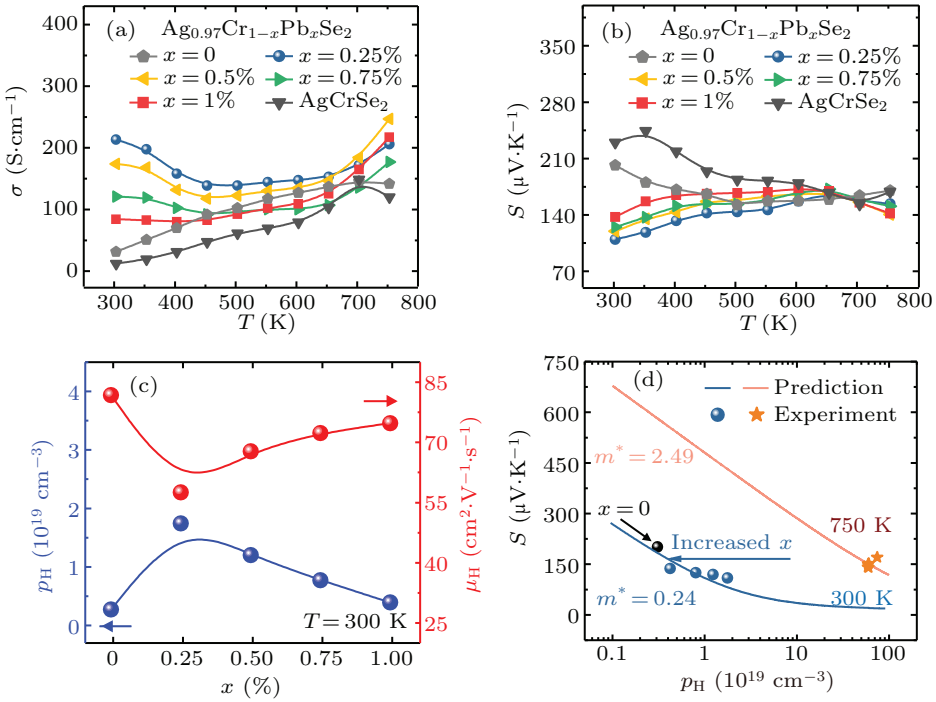


Fig. 2. Temperature-dependent (a) electrical conductivity, (b) Seebeck coefficient, (c) Hall carrier concentration and Hall mobility as a function of x at 300 K and (d) Seebeck coefficient versus Hall carrier concentration for $Ag_{0.97}Cr_{1-x}Pb_xSe_2$ and pristine $AgCrSe_2$ samples.

Based on the S and p_H, the temperature-dependent m^* is calculated as presented in Fig. 3(a). The m^* rises with the temperature, probably due to the increase in band gap caused by thermal expansion,[46] and the estimated E_{def} decreases with the increasing temperature. The similar trend can be found in $MnGeTe_2$,[47] Cu_2S and Cu_2Se.[48] On the basis of the predicted m^* and E_{def}, theoretical PF curves at different temperatures can be calculated, which are displayed in Fig. 3(b). The value of the horizontal coordinate corresponding to the peak PF is the $p_{H,opt}$, which is shown as a solid blue line in the figure, showing a strong correlation with temperature. Obviously, a high PF can be obtained at room temperature when the p_H is close to 5.5×10^{18} cm^{-3}, while at 750 K, the p_H close to 3×10^{20} cm^{-3} is required. Only when the measured p_H is temperature-dependent and matches the $p_{H,opt}$ value, a high PF value can be attained. The $p_{H,opt}$ is compared with the measured p_H, as shown in Fig. 3(c). It can be seen that Pb doping enhances the p_H of pristine $Ag_{0.97}CrSe_2$ at room temperature, while suppressing the rapid growth trend at a higher temperature, thereby optimizing the p_H in the full temperature region.

In order to understanding the underlying principle of p_H optimization, the ionization energy (E_A) of the impurity defects can be obtained by the following equations:

$$p_H = \left(\frac{N_A N_V}{4}\right)^{1/2} \exp\left(-\frac{E_A}{k_B T}\right), \tag{4}$$

$$N_V = 2\frac{(2\pi m^* k_B T)^{3/2}}{h^3}, \tag{5}$$

where N_A is the acceptor concentration, N_V is the density of states near the valence band maximum, and E_A is the ionization energy. We calculate the E_A for all samples, as shown in Fig. 3(d). A higher slope of the line means a higher ionization energy. For the pristine $Ag_{0.97}CrSe_2$, the E_A of ~ 0.23 eV implies that the defect level is situated at the center of the band gap ($E_g \sim 0.49$ eV).[28] The deep-level impurity states are formed due to the occupation of Cr vacancies by Ag (Ag_{Cr}), even if the sample is in a poor-Ag state, and they are continuously ionized with the increasing temperature, resulting in an

elevated p_H. Such a high E_A leads to a low room-temperature $p_H \sim 3 \times 10^{18}$ cm^{-3}, deviating from the predicted $p_{H,opt}$. Simultaneously, the rapidly increasing p_H gradually becomes higher than the $p_{H,opt}$ in the medium and high-temperature regions, leading to the deterioration of the electrical properties. The Pb occupying Cr sites not only significantly increases the p_H at room temperature, but also inhibits the deep-level defects of Ag_{Cr}, thus reducing the E_A. Notably, with further increase of the Pb, the E_A exhibits a slight increase, which is attributed to the solubility limit restricting the occupation of Cr sites by Pb^{2+} and the more exposed Cr vacancies exacerbate the formation of Ag_{Cr} defects. Benefiting from the acceptor effect of Pb^{2+} and the reduced ionization energy, the room-temperature p_H is greatly enhanced. Moreover, with the defect level completely ionized, the curve of p_H tends to be flat, approaching the optimal value. The sudden rise of p_H at high temperatures may be because of the bipolar effect.

As illustrated in Fig. 4(a), the temperature-dependent μ_H decreases with the increasing temperature via $\mu_H \sim T^{-1.5}$, which indicates that acoustic phonons dominate the charge carrier scattering and the Pb doping will not change the scattering mechanism. The p_H dependent μ_H and PF at 300 K, 450 K and 750 K are displayed in Figs. 4(b) and 4(c). Apparently, the experimental μ_H values correspond well with the predicted. Benefiting from the optimized p_H and μ_H, the PF is close to the predicted optimal value shown in Fig. 4(c). The PF of all samples is shown in Fig. 4(d). Clearly, the PF has been considerably improved. Both the samples of $x = 0.25\%$ and $x = 0.5\%$ show a large increase in PF over the whole temperature range. Eventually, the highest PF value increases from ~ 340 μW·m^{-1}·K^{-2} to ~ 500 μW·m^{-1}·K^{-2}, which is higher than the majority of previous reports (see Fig. S5),[29,36,37,40] illustrating that the Pb doping can effectively enhance the electrical properties.

Temperature-dependent thermal conductivity (κ) and lattice thermal conductivity (κ_L) are displayed in Fig. 5(a). The κ_L is calculated by subtracting the electronic component via the Wiedemann–Franz law ($\kappa_e = L\sigma T$) from the total κ. Due to the superionic transition at ~ 450 K, the κ decreases sharply to 0.5 W·m^{-1}·K^{-1} and then increases slowly, which is a typical feature of $AgCrSe_2$ material. The κ_L fitted according to the Debye–Callaway model is shown in Fig. 5(b). The inapplicability of the model reveals that the ultra-low κ_L of $Ag_{0.97}Cr_{1-x}Pb_xSe_2$ is mainly due to its intrinsic liquid-like effect.[29] The strong phonon scattering in $AgCrSe_2$ is one of the sources of its low κ_L.[49,50] As displayed in Fig. S6, the mean free paths of the Pb-doped samples are all reduced, indicating that the Pb doping can enhance phonon scattering and promote the reduction of the κ_L. Therefore, the κ_L of all Pb-doped samples is lower than that of the pristine $Ag_{0.97}CrSe_2$.

On the basis of the calculated PF and the estimated average of the κ as displayed in red background in Fig. 5(a), the p_H dependent zT can be estimated as shown in Fig. 5(c). Obviously, the zT is close to the optimal value at different temperatures, indicating that the p_H in this work approaches the optimal value. Consequently, the temperature-dependent zT values for pristine and Pb-doped samples are shown in Fig. 5(d). Benefiting from the optimized $p_{H,opt}$ and the ultralow κ_L, the Pb-doped sample ($x = 0.5\%$) shows a high zT value of ~ 0.51 at 750 K.

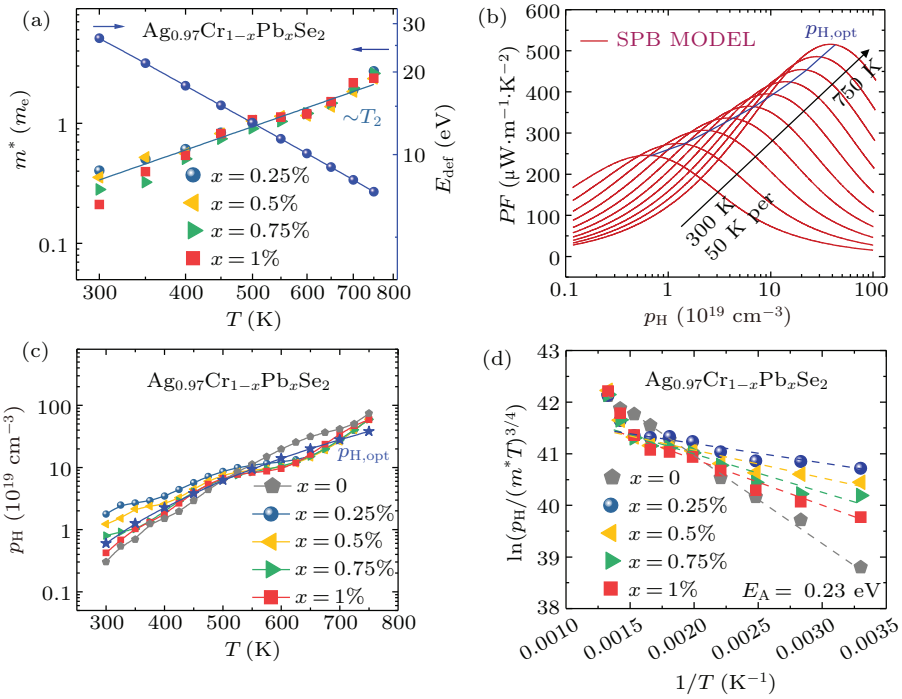


Fig. 3. (a) The density of state effective mass and deformation potential coefficient versus temperature for $Ag_{0.97}Cr_{1-x}Pb_xSe_2$ samples, (b) the power factor versus Hall carrier concentration at different temperatures, (c) the Hall carrier concentration versus temperature with the optimal carrier concentration and (d) the determination of ionization energy (E_A) for $Ag_{0.97}Cr_{1-x}Pb_xSe_2$ samples.

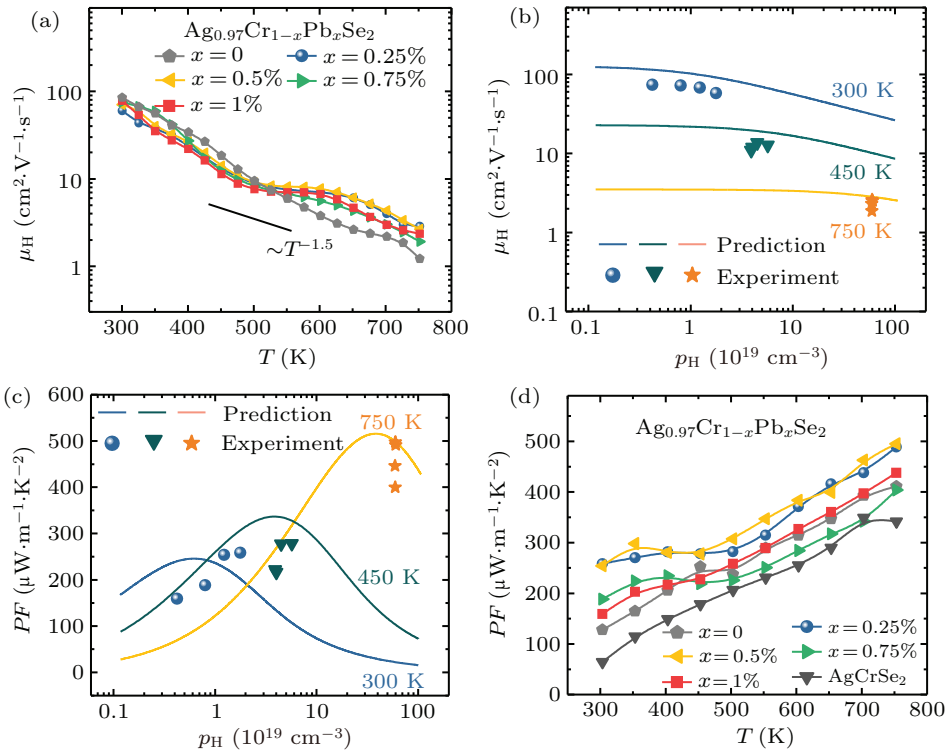


Fig. 4. (a) Temperature-dependent Hall mobility for $Ag_{0.97}Cr_{1-x}Pb_xSe_2$ samples. (b) Hall mobility, (c) power factor versus Hall carrier concentration at 300 K, 450 K and 750 K and (d) temperature-dependent power factor for $Ag_{0.97}Cr_{1-x}Pb_xSe_2$ and pristine $AgCrSe_2$ samples.

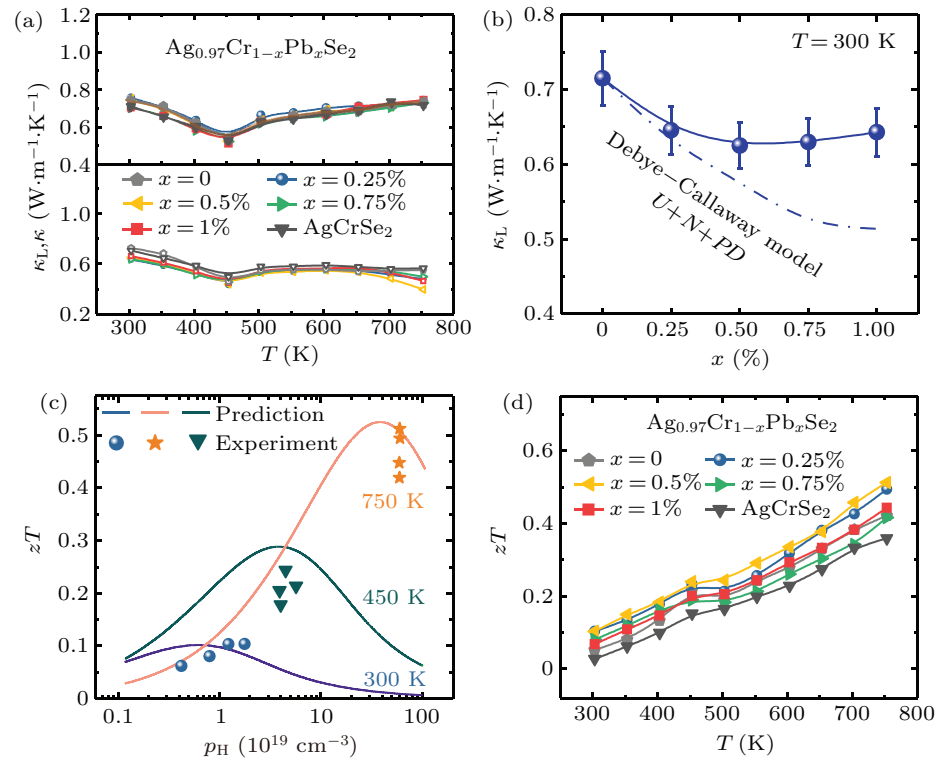


Fig. 5. (a) The temperature-dependent total, lattice thermal conductivity, (b) lattice thermal conductivity as a function of x at room temperature, compared with the Debye–Callaway model predicted result for $Ag_{0.97}Cr_{1-x}Pb_xSe_2$ compounds, (c) zT versus the Hall carrier concentration and (d) temperature-dependent zT for $Ag_{0.97}Cr_{1-x}Pb_xSe_2$ and pristine $AgCrSe_2$ compounds.

4. Conclusions

Thermoelectric transport properties of $Ag_{0.97}Cr_{1-x}Pb_xSe_2$ are systematically investigated in this work. We optimize the p_H in a broad temperature region by inducing Pb into Cr sites to suppress the intrinsic Ag_{Cr} deep-level impurity states. As the acceptor impurity, the Pb^{2+} occupies the Cr sites and increases the p_H at room temperature from $\sim 3 \times 10^{18}$ cm^{-3} to $\sim 1.77 \times 10^{19}$ cm^{-3}. Moreover, the

rapid increase in p_H at medium and high temperatures is suppressed due to the sharp decrease in ionization energy, approaching the optimal $p_{H,opt}$ curve. The optimized p_H leads to a steady increase in *PF* over the whole temperature range, and the maximum *PF* elevates from ~ 340 $\mu W \cdot m^{-1} \cdot K^{-2}$ to ~ 500 $\mu W \cdot m^{-1} \cdot K^{-2}$. Simultaneously, the Pb doping introduces additional point defects to scatter phonons that reduces the κ_L to ~ 0.4 $W \cdot m^{-1} \cdot K^{-1}$ at 750 K. Synergistic optimized electrical properties and reduced κ_L, a high peak $zT \sim 0.51$ is obtained in $Ag_{0.97}Cr_{0.995}Pb_{0.005}Se_2$ at 750 K. The current finding demonstrates that the intrinsic Ag_{Cr} deep-level defects can be suppressed by the Pb doping in $AgCrSe_2$, which provides a useful guidance for other thermoelectric materials.

See the supplementary material for SPB model simulation; Debye–Callaway model simulation; table with density for $Ag_{0.97}Cr_{1-x}Pb_xSe_2$; thermoelectric properties of Ag_yCrSe_2 samples; the enlarged XRD patterns along the [009] direction; the Lorenz number, the electrical thermal conductivity; thermal diffusivity; the property comparisons of this work and other $AgCrSe_2$-based thermoelectric materials; the mean free path.

Acknowledgements

Project supported by the National Key Research and Development Program of China (Grant Nos. 2018YFA0702100 and 2022YFB3803900), the Joint Funds of the National Natural Science Foundation of China and the Chinese Academy of Sciences (CAS)' Large-Scale Scientific Facility (Grant No. U1932106), and the Sichuan University Innovation Research Program of China (Grant No. 2020SCUNL112).

References

[1] Bell L E 2008 *Science* **321** 1457
[2] Pei Y Z, Gibbs Z M, Gloskovskii A, Balke B, Zeier W G and Snyder G J 2014 *Adv. Energy Mater.* **4** 1400486
[3] Heremans J P, Jovovic V, Toberer E S, Saramat A, Kurosaki K, Charoenphakdee A, Yamanaka S and Snyder G J 2008 *Science* **321** 554
[4] Qin B C, Hu X G, Zhang Y, Wu H J, Pennycook S J and Zhao L D 2019 *Adv. Electron Mater.* **5** 1900609
[5] Jiang B B, Wang W, Liu S X, Wang Y, Wang C F, Chen Y N, Xie L, Huang M Y and He J Q 2022 *Science* **377** 208
[6] Perunnal S, Roychowdhury S, Negi D S, Datta R and Biswas K 2015 *Chem. Mater.* **27** 7171
[7] Zhang J W, Song L R, Pedersen S H, Yin H, Hung L T and Iversen B B 2017 *Nat. Commun.* **8** 13901
[8] Wood M, Kuo J J, Imasato K and Snyder G J 2019 *Adv. Mater.* **31** 1902337
[9] Wang H, Chen J, Lu T Q, Zhu K J, Li S, Liu J and Zhao H Z 2018 *Chin. Phys. B* **27** 047212
[10] Xia K Y, Hu C L, Fu C U, Zhao X B and Zhu T J 2021 *Appl. Phys. Lett.* **118** 140503
[11] Yan X A, Joshi G, Liu W S, Lan Y C, Wang H, Lee S, Simonson J W, Poon S J, Tritt T M, Chen G and Ren Z F 2011 *Nano Lett.* **11** 556
[12] Zhang Q, Song Q C, Wang X Y, Sun J Y, Zhu Q, Dahal K, Lin X, Cao F, Zhou J W, Chen S, Chen G, Mao J and Ren Z F 2018 *Energy Environ. Sci.* **11** 933
[13] Zhu H, Sun W H, Armiento R, Lazic P and Ceder G 2014 *Appl. Phys. Lett.* **104** 082107
[14] Gayner C and Amouyal Y 2020 *Adv. Funct. Mater.* **30** 1901789
[15] Zhang X Y, Li J, Wang X, Chen Z W, Mao J J, Chen Y and Pei Y Z 2018 *J. Am. Chem. Soc.* **140** 15883
[16] Li J, Chen Z W, Zhang X Y, Yu H L, Wu Z H, Xie H Q, Chen Y and Pei Y Z 2017 *Adv. Sci.* **4** 1700341
[17] Anand S, Wood M, Xia Y, Wolverton C and Snyder G J 2019 *Joule* **3** 1226
[18] Li W, Lin S Q, Weiss M, Chen Z W, Li J, Xu Y D, Zeier W G and Pei Y Z 2018 *Adv. Energy Mater.* **8** 1800030
[19] Zhao K P, Qiu P F, Shi X and Chen L D 2020 *Adv. Funct. Mater.* **30** 1903867
[20] Liu H L, Yuan X, Lu P, Shi X, Xu F F, He Y, Tang Y S, Bai S Q, Zhang W Q, Chen L D, Lin Y, Shi L, Lin H, Gao X Y, Zhang X M, Chi H and Uher C 2013 *Adv. Mater.* **25** 6607
[21] Fujikane M, Kurosaki K, Muta H and Yamanaka S 2005 *J. Alloys Compd.* **393** 299
[22] Pei Y Z, Heinz N A and Snyder G J 2011 *J. Mater. Chem.* **21** 18256
[23] Lin S Q, Li W, Li S S, Zhang X Y, Chen Z W, Xu Y D, Chen Y and Pei Y Z 2017 *Joule* **1** 816
[24] Liu J Y, Chen L and Wu L M 2022 *Nat. Commun.* **13** 2966
[25] Yang L, Chen Z G, Han G, Hong M, Zou Y C and Zou J 2015 *Nano Energy* **16** 367
[26] Liu W D, Yang L, Chen Z G and Zou J 2020 *Adv. Mater.* **32** 1905703
[27] Xiao X X, Xie W J, Tang X F and Zhang Q J 2011 *Chin. Phys. B* **20** 087201
[28] Bhattacharya S, Bohra A, Basu R, Bhatt R, Ahmad S, Meshram K, Debnath A K, Singh A, Sarkar S K, Navneethan M, Hayakawa Y, Aswal D K and Gupta S K 2014 *J. Mater. Chem. A* **2** 17122
[29] Tang M J, Chen Z Y, Guo X M, Zhang F J, Zhong Y, Liu H T, Kang B and Ang R 2020 *ACS Appl. Mater. Interfaces* **12** 36347
[30] Maignan A, Guilmeau E, Gascoin F, Breard Y and Hardy 2012 *Sci. Technol. Adv. Mater.* **13** 053003
[31] Engelsman F M R, Wiegers G A, Jellinek F and Van Laar B 1973 *J. Solid State Chem.* **6** 574
[32] Van Der Lee A and Wiegers G A 1989 *J. Solid State Chem.* **82** 216
[33] Gautam U K, Seshadri R, Vasudevan S and Maignan A 2002 *Solid State Commun.* **122** 607
[34] Yano R and Sasagawa T 2016 *Cryst. Growth Des.* **16** 5618
[35] Ding J X, Niedziela J L, Bansal D, Wang J L, He X, May A F, Ehlers G, Abernathy D L, Said A, Alatas A, Ren Y, Arya G and Delaire O 2020 *Proc. Natl. Acad. Sci. USA* **117** 3930
[36] Wu D, Huang S Z, Feng D, Li B, Chen Y X, Zhang J and He J Q 2016 *Phys. Chem. Chem. Phys.* **18** 23872
[37] Tang M J, Chen Z Y, Yin C, Lin L W, Ren D, Liu B, Kang B and Ang R 2020 *Appl. Phys. Lett.* **116** 163901
[38] Pei Y Z, May A F and Snyder G J 2011 *Adv. Energy Mater.* **1** 291
[39] Zhao W Y, Liu Z Y, Wei P, Zhang Q J, Zhu W T, Su X L, Tang X F, Yang J H, Liu Y, Shi J, Chao Y M, Lin S Q and Pei Y Z 2017 *Nat. Nanotechnol.* **12** 55
[40] Tang M J, Li J, Wang Y D, Gong H J, Huang Y P, Kang B, Zhang K and Ang R 2021 *Appl. Phys. Lett.* **118** 193902
[41] Lu M, Zhang X, Zhang Y, Guo J, Shen X Y, Yu W W and Rogach A L 2018 *Adv. Mater.* **30** 1804691
[42] He F Q, Song E H, Zhou Y Y, Ming H, Chen Z T, Wu J C, Shao P S, Yang X F, Xia Z G and Zhang Q Y 2021 *Adv. Funct. Mater.* **31** 2103743
[43] Ravichandran K, Nithiyadevi K, Gobalakrishnan S, Raman R G, Baneto M, Swaminathan K and Sakthivel B 2016 *Mater. Technol.* **31** 865
[44] Cai J F, Yang J X, Liu G Q, Xu L, Wang X M, Hu H Y, Tan X J and Jiang J 2022 *Adv. Energy Mater.* **12** 2103287
[45] Wei T R, Tan G J, Wu C F, Chang C, Zhao L D, Li J F, Snyder G J and Kanatzidis M G 2017 *Appl. Phys. Lett.* **110** 053901
[46] Li W, Zhou B Q, Li J, Zhu S Y and Li J 2018 *J. Alloys Compd.* **753** 93
[47] Zhou B Q, Li W, Wang X, Li J, Zheng L T, Gao B, Zhang X Y and Pei Y Z 2019 *Sci. China Mater.* **62** 379
[48] Liu W D, Yang L, Chen Z G and Zou J 2020 *Adv. Mater.* **32** 1905703
[49] Xie L, Wu D, Yang H L, Yu Y, Wang Y F and He J Q 2019 *J. Mater. Chem. C* **7** 9263
[50] Wang C and Chen Y 2020 *Npj Comput. Mater.* **6** 26